

# Dimensioning and Evaluation of the Elastic Element in a Variable Torsion Stiffness Actuator\*

J. Schuy<sup>1</sup>, P. Beckerle<sup>1,4</sup>, J. Faber<sup>2</sup>, J. Wojtus<sup>3,4</sup>, S. Rinderknecht<sup>1</sup> and O. v. Stryk<sup>3,4</sup>

**Abstract**— Variable stiffness joints are essential for robots or biomechanical applications to generate torque with sufficient compliance to ensure safety simultaneously. This paper presents the dimensioning of the elastic element for an actuator with Variable Torsion Stiffness (VTS). Analytical and finite element calculations are compared to experimental evaluation of a splined shaft profile realized in a prototype implementation. Based on simplifications and effects in the real test-rig the results show similar behaviour. Furthermore, an analytical and finite element investigation of four cross-sections with torsional load illustrate optimal utilization of cylindrical geometries considering the torsional stress. In contrast, the low stressed edges of uncylindrical cross-sections are adequate areas to bear additional stresses.

## I. INTRODUCTION

Series elastic joint concepts are an important field in robotic and prosthetic research due to safety aspects in mutual human-machine interaction and increased efficiency requirements in mobile appliances. Such joint concepts enable safer and flexible applications, as they can behave compliant interacting with humans, are able to store energy and thus optimize motion efficiency. For the latter purpose adjusting the stiffness is advantageous, since the natural frequency of the drive train and the frequency of the desired trajectory can be matched [1], [2]. With the Series Elastic Actuator (SEA) [1] and the Mechanical Impedance Adjuster (MIA) [3] robotic joints with variable stiffness were introduced in the 1990s. Since then, a high number of alternative concepts were proposed and later categorized in four groups considering the principle of stiffness variation in [4]. Those are equilibrium-controlled, antagonistic-controlled, structure-controlled and mechanically controlled stiffness. Changing the equilibrium position of a spring, the SEA belongs to the first group. Combining two SEAs in a kinematic setup working against each other leads to antagonistic-controlled approaches like in AMASC [5]. Since the equilibrium-controlled solutions require power to simulate a virtual spring while the actuators work against each other in the antagonistically-controlled ones, energy is dissipated during operation in both. Hence, the majority of present designs for

variable stiffness joints belong to the structure-controlled and mechanically controlled group. Structure-controlled devices change the system stiffness by manipulating the structure of an elastic element, while mechanically controlled ones adjust it by pretension as MACCEPA [2]. To modify the physical structure the moment of inertia or the effective length can be altered. Another possibility is to manipulate the material modulus. Van Ham [4] associates beneficial characteristics like broad stiffness bandwidth and high dynamic behavior with structure controlled-stiffness concepts. Further, an independent control of compliance and equilibrium position is possible. Exemplary to store energy with a structure-controlled stiffness, van Ham presents a leaf spring for an elastic element. While turning orientation of a beam, the moment of inertia is changing thus the element stiffness varies. Concepts like JackSpring<sup>TM</sup> [6] and MIA consist of changing the effective length. JackSpring<sup>TM</sup> is based on a helical spring with a adjustable lead screw to vary the number of active coils and thus the effective length. In MIA a leaf spring is connected to a joint by a wire and pulley. A motorized slider changes the effective length of the spring. The Variable Torsion Stiffness (VTS) presented in [7] and investigated in [8] is also characterized by varying the effective length. Contrary to MIA and JackSpring<sup>TM</sup>, the VTS geometry of the elastic element is cylindrical and the stiffness is changed via a relocatable counter bearing.

After introducing the basic functional design of the VTS and analytical dimensioning of an elastic element, potential designs of cross-sections are compared analytically in Section II. In Section III, the realized prototype is evaluated by analyzing static experiments regarding real stiffness behavior. Subsequently, in a finite element calculation the stiffness of the realized prototype is evaluated and compared to the analytical and experimental method. After analyzing the potential designs regarding structural load behavior in Section IV, a conclusion and an outlook is given in Section V.

## II. ANALYTICAL DIMENSIONING

The principal functionality of a VTS actuator is shown in Figure 1. The torque  $\tau_i$  moving the link is applied to the torsional elastic element by actuator 1 inducing a torsional deflection  $\vartheta$  corresponding to the difference of the output angle  $\varphi_o$  and the input angle  $\varphi_i$ . Actuator 2 adjusts the torsional stiffness of the drive train  $k_{vts}(x)$  by varying the effective length  $x$  of the elastic element via the location of a counter bearing. Hence, the actuation of joint positioning and stiffness control are separated and the stiffness adjustment and joint motion can be conducted independently from each

\*This work was funded by Forum for Interdisciplinary Research of Technische Universität Darmstadt.

<sup>1</sup> Institute for Mechatronic Systems, Department of Mechanical Engineering, Technische Universität Darmstadt, lastname@ims.tu-darmstadt.de

<sup>2</sup> Institute for Lightweight Design and Construction, Technische Universität Darmstadt, jakob.faber@klub.tu-darmstadt.de

<sup>3</sup> Simulation, Systems Optimization, and Robotics Group, Department of Computer Science, Technische Universität Darmstadt, lastname@sim.tu-darmstadt.de

<sup>4</sup> Member, IEEE

other during operation. A basic model of the drive train's behaviour is given by

$$\tau_t = k_{vts}(x) \vartheta = \frac{G I_t(x)}{x} (\varphi_o - \varphi_i). \quad (1)$$

### A. Basic Functional Design

In [7] the geometric design of the elastic element is determined based on a required stiffness range between  $50 \frac{\text{Nm}}{\text{rad}}$  and  $350 \frac{\text{Nm}}{\text{rad}}$  according to [2] and an utilized length of  $x_{min} \leq x \leq x_{max}$  with  $x_{max} = l = 0.01$  m. Assuming a thick-walled hollow cylinder with ratio factor  $\lambda$  between inner radius  $r$  and outer radius  $R$  of the elastic element, the torsional moment of inertia

$$I_t = \frac{\pi(R^4 - r^4)}{2} = \frac{\pi}{2}(1 - \lambda^4)R^4 \quad (2)$$

is replaced in  $k_{vts}(x)$  of equation in (1) resulting in

$$k_{vts} = \frac{\pi G(1 - \lambda^4)R^4}{2x}. \quad (3)$$

To specify the geometry for a maximum required stiffness at minimum active length, (3) is rearranged leading to

$$R = \sqrt[4]{\frac{2 k_{vts,max} x_{min}}{\pi G(1 - \lambda^4)}}. \quad (4)$$

In order to realize the required stiffness range, an outer radius  $R = 9$  mm is determined in [7] based on (3) and assuming that the elastic element is manufactured from polyethylene ( $G = 0.387$  GPa) and  $\lambda = 0.5$ .

### B. Comparison of Geometries

Beyond cylindrical geometries A, other cross-sections of the elastic elements can be taken into account for practical implementation, given in Figure 2. Hence, (3) is adapted for a quadratic B, hexagonal C and octagonal D cross-section leading to

$$k_{vts} = \frac{G c_g b^4}{x}, \quad (5)$$

based on the torsional moments of inertia as given in [9]. In this,  $b$  represents the distance between the parallel edges of the cross-section, while the geometry factor  $c_g$  is listed in Table I. Hence the design equation in analogy to (4) is given by

$$b = \sqrt[4]{\frac{2 k_{vts,max} x_{min}}{G c_g}}. \quad (6)$$

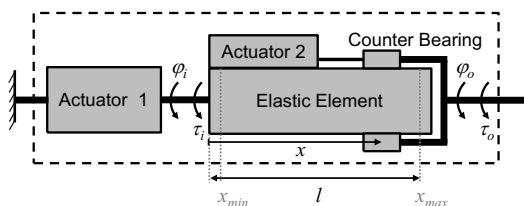


Fig. 1. Sketch of the principle VTS functionality from [7].

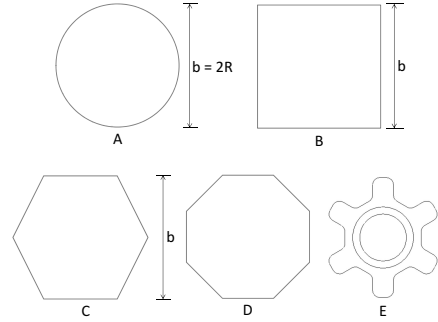


Fig. 2. Investigated cross-sections: cylindrical A, quadratic B, hexagonal C, octagonal D and splined shaft E

Considering polyamide with  $G = 0.68$  GPa as the material for the elastic element and  $x_{min} = 0.01$  m, the geometry parameters  $R$  and  $b$  resulting from (4) and (6) for  $k_{vts,max} = 350 \frac{\text{Nm}}{\text{rad}}$  can be calculated and are given in Table I. For all investigated cross-sections the maximum active length  $l_{k,min}$  required to realize the minimum stiffness is 0.07 m. It becomes distinct, that the dimensions of all cross-sections are comparable. Therefore, the geometry can be chosen due to practical reasons like the torque input and output realization or manufacturing issues. Beyond the low required length  $l_{k,min}$ , geometries with square, hexagonal or octagonal cross-section might increase system integration for application in a prosthetic knee joint as proposed in [7], as torque input and output might be realized by the edges of the cross-section directly. This analytical study is based on a cylindrical profile in contrast to the splined shaft profile E, used in the experimental evaluation. Thus, the stiffening fitting rails are not considered. Cross-sections have a torsional resistance factor  $c_r$ , presented in [9]. From this and

$$\sigma_{max} = \frac{\tau_t}{c_r b^3}, \quad (7)$$

a cross-section typical maximum shear stress  $\sigma_{max}$  results listed in Table I. It becomes distinct, that the distribution of the material stress is improved, if the geometry approximates a cylindrical geometry. Hence, the material utilization increases and installation space decreases. The normalized shear stresses of the investigated cross-sections are given in Table I.

TABLE I  
COMPARISON OF ELASTIC ELEMENT GEOMETRIES.

Type	Cylindrical	Square	Hexagonal	Octagonal
Geo. \mm	$R = 7.8$	$b = 14.1$	$b = 14.8$	$b = 15.1$
$c_g$	$\pi/32$	0.141	0.115	0.108
$c_r$	$\pi/16$	0.208	0.188	0.185
$\frac{\sigma_{max}}{\sigma_{cylinder,max}}$	100%	128%	122%	117%

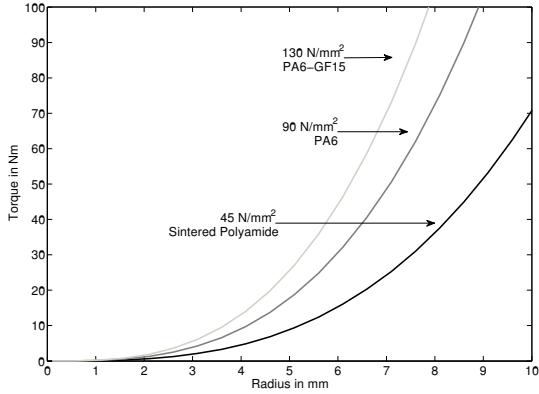


Fig. 3. Transmittable torque of a cylindrical cross-section depending on radius and material strength.

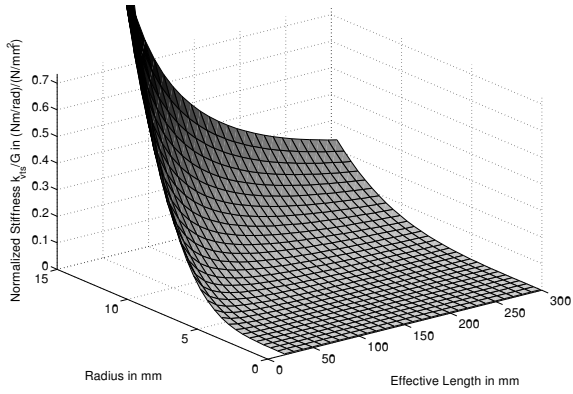


Fig. 4. Radius to length combinations for different stiffness ranges and materials.

### C. Mechanical Strength Dimensioning

Considering a dimensioning regarding mechanical strength of a cylindrical cross-section in correlation with material and critical torque, the required minimum cross-section radius with collapse safety is depicted in Figure 3. It presents curves of a cylindrical cross-section for different plastics, exemplary. By considering minimum radius and defined material, the minimum and maximum effective lengths are resulting depending on the desired range of stiffness as plotted in Figure 4. This approach is practicably analogue to the other cross-sections by considering the factors, given in Table I.

## III. EXPERIMENTAL EVALUATION

The realization of the elastic element as a prototype is shown in Figure 5. On the left side of the sketch, the flange connecting the element to the drive side adapter by screws can be seen. In Figure 6 on top, the drive side adapter is depicted on the left side of the elastic element.

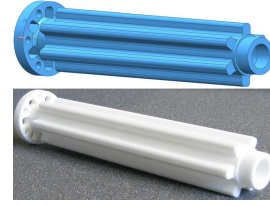


Fig. 5. Elastic element - *Top*: CAD-model, *Bottom*: Prototype.

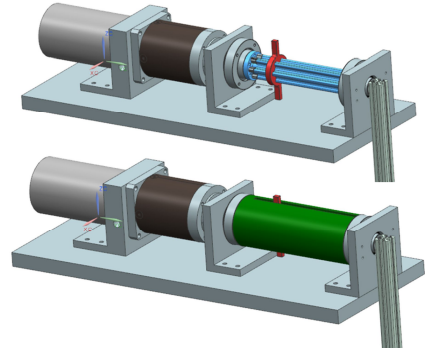


Fig. 6. Test-rig CAD-model - *Top*: without downforce shell, *Bottom*: with downforce shell.

Furthermore, holes allow the drive side adapter to go through the flange, if the counter bearing is located at  $x = 0$  m. In this case, a rigid connection of the output to the input side is provided. Along the elastic element, six evenly distributed fitting rails are used to transfer the torque to the output side. On the very right side of the picture one of the inner bearing seats is shown, which does not influence the stiffness parameters. The elastic element in the prototype differs from the ideal hollow-cylinder determined in [7], since it is manufactured from laser-sintered polyamide PA2200 instead of polyethylene and its geometry is varied. Increasing the outer radius to  $R = 11$  mm is required to provide an appropriate interface to the fitting rails for



Fig. 7. Real Test-rig.

torque transmission. Further, modification to  $\lambda = 0.791$  and  $l = 0.16$  m is necessary to match the required stiffness bandwidth, although the outer radius is increased.

The prototypical test rig realizing a drive train with the elastic element is shown in Figure 6. On its left side the DC motor actuating the drive train is depicted. The applied torque is transmitted to the input side by a planetary gear box and transferred to the elastic element by a bellows coupling at the drive side adapter. To adjust the effective length and thus the stiffness of the elastic element contained in a slotted tube, a relocatable slider is used. In combination with this slider, the slotted output tube implements the counter bearing of the VTS drive train. It is rigidly connected to the pendulum on the right hand of the sketch. For the acquisition of the angular positions and velocities at the VTS input side, an optical encoder mounted on the DC motor is used. As the interface between the motor and the elastic element can be assumed to be rigid considering torsion, the angle  $\varphi_m$  from the motor shaft can be converted to  $\varphi_i$  at the VTS input by the gear ratio  $i_g = 80$ . Further, the position  $\varphi_o$  of the pendulum is acquired using a rotary potentiometer at the output side. A static experiment is performed to evaluate the stiffness characteristics of the element: Corresponding to different stiffness values, the active length  $x$  is set to values between 0.011 m and 0.151 m in steps of 0.02 m and a final step to  $x = 0.166$  m. At every active length the pendulum is positioned at specific angles statically, the input and output angles are measured and the torque  $\tau_g$  due to gravity and mass of the pendulum is determined as in [8]. This torque is calculated based on the link side dynamics

$$I_{rp} \ddot{\varphi}_o + m_p g \alpha l_p \sin(\varphi_o) = -\tau_t, \quad (8)$$

by  $\tau_g = m_p g \alpha l_p \sin(\varphi_o)$ , as the influence of inertia can be neglected in the static case. Hence, the current stiffness  $k_{vts}$  corresponding to the slope of the torque-angle characteristics can be evaluated by rearranging (1) to

$$k_{vts} = \frac{\tau_g}{\varphi_i - \varphi_o}, \quad (9)$$

and substituting the values of  $\tau_g$ ,  $\varphi_i$  and  $\varphi_o$ . The stiffness characteristics determined in these experiments at specific active lengths are shown in Figure 8. It becomes distinct, that the torque-angle characteristics and thus the stiffness of the elastic element can be assumed to be linear at those lengths. The other investigated active length settings, not presented in Figure 8 shows comparable behavior. Hence, a linear stiffness model  $k_{vts}(\varphi_o) = k_{off} + k_{lin} \varphi_o$  is estimated at each investigated active length using least squares regression. As the parameters  $k_{off}$  describing constant offsets are close to zero, those are not considered any further. The stiffness-length characteristics determined from the linear coefficients  $k_{lin}$  are presented in Figure 9. Comparing the experimentally determined characteristics plotted in black solid line with the ones from the analytical model plotted in black dotted line, higher values are observed in the experiment for active lengths above  $x = 0.04$  m. Below this length, the analytical solution exceeds the

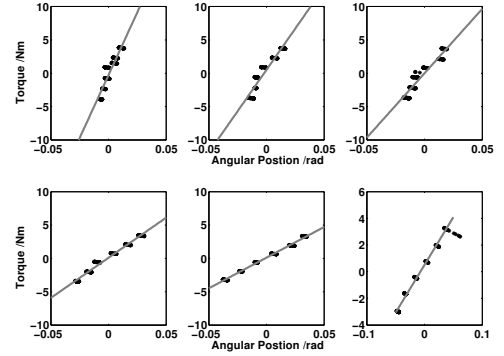


Fig. 8. Experimentally determined torque-angle characteristics at specific active lengths - *Top*:  $x = 0.011$  m, 0.031 m, 0.051 m, *Bottom*:  $x = 0.091$  m, 0.131 m, 0.166 m. Black: Experimental results, grey: Estimated characteristics.

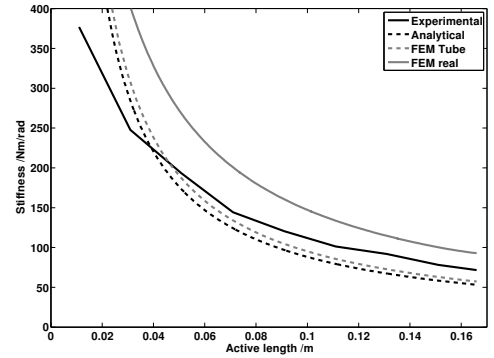


Fig. 9. Stiffness-length characteristics; experimentally determined, analytical and finite element calculated.

experimentally obtained results, as the analytical solution converges to infinity, while the real system is constrained to finite stiffness as shown in [8]. The increased stiffness of the prototype above  $x = 0.04$  m is caused by its implementation, as the elements structure is reinforced by the fitting rails. Due to this, most of the required stiffness bandwidth except of values below  $71.56 \frac{\text{Nm}}{\text{rad}}$  is covered by this element, although a minimum stiffness of  $53.13 \frac{\text{Nm}}{\text{rad}}$  is expected from analytical design. Yet, a finite element dimensioning might lead to better results providing the whole stiffness bandwidth, since the complex geometry of the prototypical implementation can be considered.

#### IV. FINITE ELEMENT EVALUATION

The finite element method (FEM) is used to investigate two main issues. First goal is an evaluation to compare and verify the stiffness analysis of experimental measurement and analytical calculation with the finite element calculation. Second goal is an investigation of component stress to deduce further potential designs.

### A. Stiffness Comparison

Investigating the first-mentioned issue, the rotation of the splined shaft profile is computed in analogy to the real setup. Yet, the finite element calculation does not consider effects like backlash and tolerances of material and manufacturing. Additional compliance exists due to further involved parts in the test-rig, presented in Section III. The calculations present subsequently rely on simplified geometries and boundary conditions to show qualitative results for comparison. Thus, a contact pressure investigation of the counter bearing is not examined at the moment. All calculations assumed ideally stiff flanges without buckling and a fixation on the drive side. The compliance in the bearing seat is considered as follows: In the area of force application, a deviation through local deflections of the fitting rails is detectable. These small deflections of about 0.8% have no relevant effect to the stiffness calculation. Considering the assumptions introduced previously, linear calculations for small displacements (quasi-static) were done. A comparison of torque application at the output flange and applied forces on the counter bearing contact areas show a good correlation regarding the torsional displacement. With equation (1), the displacements are converted to the rotational stiffness of the elastic element in Nm/rad to be comparable with the stiffness values of the experimental and analytical results. The finite element calculation result is depicted in Figure 9 in grey solid line. There, the stiffness values of the FEM are higher than the analytical results (up to 62%), mainly caused by the increased torsional moment of inertia based on the fitting rails. In comparison to the experimental result, the finite element calculated values are generally higher. However, they have a similar trend with lower deflection further away from the fixed clamp. The higher values can be attributed to the additional compliance of the test-rig, explained above. Closer to the fixed clamp, analytical calculations become singular based on a fraction in the equation for stiffness calculation. Thus, calculated stiffness values near the drive side clamp are not applicable.

### B. Design Comparison

To discover potential design solutions with comparable characteristics, the cross-sections presented in Section II, are investigated with the geometry parameters from Table I. The component stress resulting from a torque of 1 Nm is depicted in Figure 10 comparable to the typical maximum shear stress given in Table I. As shown in analytical analysis in Section II the more cylindrical cross-section exhibits the best material utilization with continuous load distribution. Furthermore, the finite element calculation illustrates obviously low stressed bright parts, the edges. Those are found to be adequate areas to bear additional stresses, for example as contact areas of the relocatable slider, presented in Section III. The structural stress analysis exemplifies equivalent findings to the other investigated cross-sections. The fitting rails depicted in Figure 11 are not mainly involved to load stress. A modeling of force application to the stress

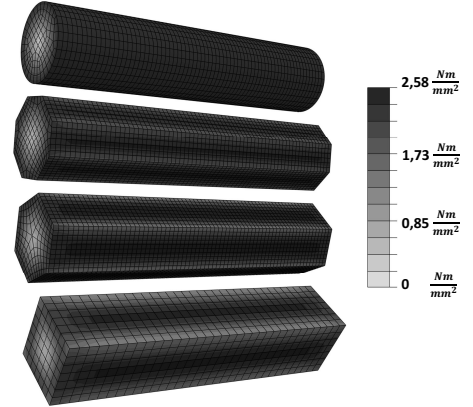


Fig. 10. Structural load analysis of investigated cross-sections.



Fig. 11. Structural load analysis of the prototype.

transfer areas and detailed examination of stress peaks as well as superimposed stress is necessary.

## V. CONCLUSIONS

In Section II, the analytical dimensioning of elastic elements with desired stiffness ranges for VTS drive trains is presented. A comparison of four cross-sections considering basic applicability of torsional stress is realized. Subsequently, an analytical stress calculation shows optimal utilization of geometry and material is achieved by using a cylindrical cross-section as expected for torsional loads. In this, an oversizing rating can be determined for equal loads with the introduced relation factors. Thus, a comparability is created. Further, a method for dimensioning with minimum radius, specific material and stiffness range and safety against failure is presented. The realization of the elastic element of VTS in a prototype is presented and the experimental evaluation of stiffness investigation in this test-rig is given. In Section III, a comparison exhibits value differences between analytical, experimental and finite element investigation. The constant deviation of the analytical investigation is based on the simplification to a cylindrical cross-section without observing the fitting rail geometry of the real cross-section. Even the finite element calculation illustrates deviations to the experimental investigation through simplified modeling

and other effects in the real test-rig setup. Analytical dimensioning for simple, defined cross-sections is sufficient and can be transferred to other cross-section by the introduced factors. By using a complex design, the torsional moment of inertia and additional compliances of the real system have to be observed to obtain the desired global range of stiffness. For the deduction of mechanical designs for robotic and biomechanical systems, the cross-sections introduced in Section II are analyzed by finite element method. The results are related to the analytical findings and exemplify low stressed edges. Thus, these areas are usable for application of output forces to the relocatable slider, introduced in Section III. Consequently, the full geometry is involved by the superimposed stress consisting of torsional load of drive train and output forces. Currently, the prototyped design is practicable to investigate the technology of variable torsion stiffness. Yet, a optimization of the elastic element based on the results of this paper is possible. In next steps a geometrical optimization will be done by modeling stress transfer areas and detailed examination of stress peaks as well as superimposed stress. Potential designs are polygonal cross-sections like P4C and P3G of DIN 32711 and DIN 32712, presented in [10]. Regarding potential materials, thermoplastic polyurethane would be able to offer a possibility to do the conflict of objective related to structural strength and torsional compliance.

#### ACKNOWLEDGMENT

The authors thank Bühler Motor GmbH and National Instruments Germany for hardware donation.

#### REFERENCES

- [1] G. A. Pratt and M. M. Williamson, "Series elastic actuators," in *Proceedings of the 1995 IEEE/RSJ International Conference on Intelligent Robots and Systems*, 1995.
- [2] B. Vanderborght, R. Van Ham, D. Lefeber, T. G. Sugar, and K. W. Hollander, "Comparison of Mechanical Design and Energy Consumption of Adaptable, Passive-compliant Actuators," *The International Journal of Robotics Research*, vol. 28, pp. 90–103, 2009.
- [3] T. Morita and S. Sugano, "Design and development of a new robot joint using a mechanical impedance adjuster," in *1995 IEEE International Conference on Robotics and Automation*, 1995.
- [4] R. Van Ham, T. G. Sugar, B. Vanderborght, K. W. Hollander, and D. Lefeber, "Compliant Actuator Designs Review of Actuators with Passive Adjustable Compliance/Controllable Stiffness for Robotic Applications," *IEEE Robotics & Automation Magazine*, vol. 16, pp. 81–94, 2009.
- [5] J. W. Hurst, J. E. Chestnutt, and A. A. Rizzi, "An actuator with physically variable stiffness for highly dynamic legged locomotion," in *2004 IEEE International Conference on Robotics and Automation*, 2004.
- [6] K. W. Hollander, T. G. Sugar, and D. Herring, "Adjustable robotic tendon using a 'jack spring'<sup>TM</sup>," *Proceedings of the 2005 IEEE 9th International Conference on Rehabilitation Robotics*, pp. 113 – 118, 2005.
- [7] J. Schuy, P. Beckerle, J. Wojtusich, S. Rinderknecht, and O. von Stryk, "Conception and Evaluation of a Novel Variable Torsion Stiffness for Biomechanical Applications," in *IEEE International Conference on Biomedical Robotics and Biomechatronics*, 2012.
- [8] P. Beckerle, F. Stuhlenmiller, J. Schuy, J. Wojtusich, S. Rinderknecht, and O. v. Stryk, "Friction compensation and stiffness evaluation on a variable torsion stiffness (accepted)," in *6th International Symposium on Adaptive Motion of Animals and Machines*, 2013.
- [9] K.-H. Grote and J. Feldhusen, *Dubbel - Taschenbuch für den Maschinenbau*. Springer, 2011.
- [10] M. Ziaei and C. Grossmann, "Optimierung der Polygonprofile nach DIN 32711 und DIN 32712 zur Entwicklung einer verbesserten Norm und eines Konzeptes zur Festigkeitsberechnung von Polygon-Welle-Nabe-Verbindungen," TU Chemnitz, Germany, Tech. Rep., 2003.